Available online at www.sciencedirect.com
ScienceDirect
Trans. Nonferrous Met. Soc. China 35(2025) 3578−3594
Transactions of Nonferrous Metals Society of China
www.tnmsc.cn

Effect of natural aging and pre-aging on microstructure evolution and strengthening ability of Al−Mg−Si alloy during age hardening

Shu-hui LIU[1,2], Qing-lin PAN[3], Hong-feng HUANG[1,2], Jing WANG[4], De-gui LI[4], Zhi-xin NING[1], Li-li WEI[1,2]

1. College of Materials Science and Engineering, Guilin University of Technology, Guilin 541004, China;
2. Key Laboratory of New Processing Technology for Nonferrous Metal & Materials, Ministry of Education, Guilin University of Technology, Guilin 541004, China;
3. School of Materials Science and Engineering, Central South University, Changsha 410083, China;
4. Engineering Research Center of Advanced Aluminum Matrix Materials of Guangxi, Baise University, Baise 533000, China

Received 25 January 2024; accepted 15 November 2024

Abstract: The microstructure evolution and strengthening ability of natural aging (NA), delayed aging (DA), and DA after pre-aging (PDA) of Al−Mg−Si alloy were studied. Results show that small and unstable atomic clusters are generated during NA, leading to the formation of low-density coarse β'' and β' phases, thus reducing the strength of DA alloy. However, atomic clusters and GP zones with larger sizes and high Mg/Si molar ratio form during pre-aging treatment. They prevent the generation of clusters during NA and can serve as effective nucleation sites in subsequent artificial aging, which elevates the number density of fine β'' precipitates and improves the alloy strength. After pre-aging at 175 °C, the strengthening capacity of PDA alloy is restored, with hardness and yield strength reaching 95.1% and 101.9% of peak-aged alloy.

Key words: pre-aging; delayed aging; precipitate; microstructure evolution; strengthening ability; Al−Mg−Si alloy

1 Introduction

The 6××× aluminum alloy is broadly applied in vehicle body frames due to the high specific strength, favorable formability and reasonable weldability, which lightens the automotive structures and reduces energy consumption [1−3]. The grain-boundary strengthening, dislocation strengthening, solid-solution strengthening and precipitation strengthening are the main factors that determine the strengthening capacity of a fixed alloy. As a heat-treatable Al−Mg−Si alloy, precipitation strengthening during heat treatment is the chief hardening method due to the hindering effect of the nanoscale precipitate on dislocation movement, and the age hardening capabilities are primarily affected by the morphology of the aging precipitates [4,5]. The commonly accepted precipitation sequence of Al−Mg−Si alloy can be regarded as follows [6,7]: supersaturated solid solution → atom cluster → GP zone →β''(Mg_5Si_6) precipitate→β'(Mg_9Si_5)/U_1($MgAl_2Si_2$)/U_2($Mg_2Al_2Si_2$)/B'($Mg_9Al_3Si_7$) precipitate →β(Mg_2Si) precipitate, where β'' phase is the most effective strengthening phase [8]. To obtain high density and fine β'' phase, the aging treatment requires adjustment to ensure reasonable strengthening ability.

Generally, device scheduling and material storage-site transfer are required during heat treatment, and the alloy needs to be stored at room temperature for a time inevitably after quenching

Corresponding author: Li-li WEI, Tel: +86-13517739930, E-mail: weill@glut.edu.cn
https://doi.org/10.1016/S1003-6326(25)66900-7

and before artificial aging (AA). This delayed aging (DA) behavior, which has a parking effect, may affect the aging precipitation and thus has a significant impact on the mechanical properties [9]. For Al−Mg−Si alloys with Mg+Si content >1 wt.%, nature aging (NA) exerts a negative effect on DA alloy [10−12], otherwise, NA shows a positive effect on the subsequent AA treatment [13,14]. A study on Al−0.44Mg−0.38Si alloy treated with DA implied that the enhancing ability is improved due to the formation of clusters during NA [15], and the number density of strengthening precipitates after DA exceeds that of peak aging. Another investigation on Al−Mg−Si alloy shows that the effect of NA on AA is related to the aging temperature, i.e., NA has a negative effect when artificially aged at 180 °C [16]. With increased aging temperature to 250 °C, the microstructure of alloy becomes dominated by β'' phase, which improves the mechanical performance of the alloy.

Considerable research has been focused on DA behavior to meet the increasing requirements for the age-hardening ability of Al−Mg−Si alloy [17−19]. To mitigate the NA negative effects on strengthening performance, methods such as pre-aging (PA) treatment [20,21], addition of trace solute elements [22], adjustment of Mg/Si ratio [11], and deformation before aging treatment [1] have been adopted. Amongst them, adjusting the type or content of solute elements may affect the overall performance, especially the corrosion resistance, whereas performing deformation treatment reduces the plasticity. PA treatment is an effective way to improve the mechanical properties by modifying the microstructure [23]. Besides, PA treatment can also be performed by incorporating thermo-mechanical pre-aging process into the production line [24], which is favorable to improving the parking effect. Many researchers have examined the effect of PA treatment at 60−120 °C [18,19,23], but studies on PA at elevated temperatures remain lacking. It is well known that the movement of solute atoms is accelerated at high temperatures, promoting precipitation and reducing the aging time. Short-time high-temperature PA treatment is supposed to be an effective way to improve efficiency.

Effective information on the size and number density of solute clusters can be obtained using a three-dimensional atomic probe (3DAP) and a high-resolution transmission electron microscope (HRTEM), which is productive for exploring the strengthening ability [25,26]. Existing literature has focused on the analysis of the solute cluster morphology [27], and few studies have analyzed the contribution of pre-treatment to strength, but only the precipitation strengthening is considered [28]. ENGLER et al [20] investigated the effects of solid-solution strengthening and precipitation strengthening on the pre-aging treatment of AA6016 alloy, but the contribution of grain-boundary strengthening and dislocation strengthening was not examined. Therefore, a comprehensive pre-aging strengthening study is necessary to enrich the theoretical strengthening mechanism and improve the accuracy of strength prediction.

In the present study, a novel short-time high-temperature PA treatment was adopted to mitigate the parking effect of Al−Mg−Si alloy. The microstructure evolution of atomic cluster, GP zone, pre-β'' phase, β'' phase, and β' phase during NA, AA, DA, PA, and delayed aging after pre-aging (PDA) treatments was thoroughly characterized by 3DAP combined with TEM and HRTEM analyses. The effect of PA treatment was assessed using comprehensive theoretical calculations to determine the ability of precipitation strengthening, dislocation strengthening, and grain-boundary strengthening in different aging states. Then, the difference between the calculated strengths and experimental values was evaluated. This study improves the strength of DA alloy and enriches the theoretical study of pre-aging strengthening.

2 Experimental

2.1 Materials and heat treatment processes

The alloy-extruded profile studied in this work was produced by Guangdong Fenglu Aluminum Industry Co., Ltd., China. The chemical composition obtained from ICP 6300 instrument is shown in Table 1. Solution heat treatment was performed in an air furnace at 545 °C for 50 min followed by water quenching. After aging at different temperatures and followed by air cooling, DA and PDA alloys were obtained, and intermediate-state alloys including NA, PA, and pre-aging before natural aging (PN) alloys were prepared to systematically investigate the microstructural evolution. AA alloy with direct

artificial aging after solid solution (T6) was also prepared for comparison. Details are shown in Fig. 1, where the NA was parked at room temperature (RT) for 48 h, and PA was performed at 100, 125, 150, and 175 °C and held for 30 min, respectively.

Table 1 Chemical composition of alloy (wt.%)

Mg	Si	Mn	Cr	Fe	Cu	Ti	Zn	Al
0.68	0.94	0.53	0.11	0.25	0.04	0.09	0.08	Bal.

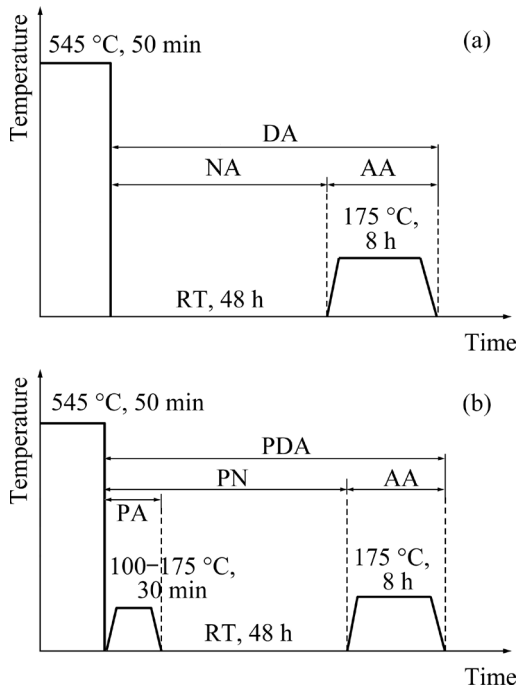

Fig. 1 Schematic diagrams of heat-treatment routes of DA (a) and PDA (b)

2.2 Performance tests

Tensile tests were performed on a WDW−100 testing machine with a tensile speed of 2 mm/min. Hardness tests were conducted on a WOLPERT 401MVD^{TM} micro-Vickers hardness tester at a load of 500 mN for a dwelling time of 15 s. The tensile and hardness tests of each sample were repeated three times and seven times, respectively. The average values of the tensile and hardness measurement results were calculated, and standard deviations were used.

2.3 Microstructure observation

Transmission electron microscopy (TEM) was used to characterize the microstructure of the alloy. TEM and HRTEM observations were conducted on an FEI F20 tester at 200 kV, which can display the size, number density, and morphology of the nanoscale-strengthening precipitates. The thickness of the test foil was determined by electron energy-loss spectrometry. The foil used for TEM observation was thinned to ~60 μm after machining and grinding, and subsequently electrolytically polished on an MTP−1A double-jet electrolytic instrument in a solution of 30 vol.% nitric acid and 70 vol.% methanol at a working temperature of about −25 °C. Image J software was used to measure the radius and length of precipitates followed by statistical analysis. Each data was obtained from at least six measured images. Electron backscatter diffraction (EBSD) samples were mechanically and electrolytically polished using a mixture of ethanol and perchloric acid, and then tested with a Zeiss Sigma 300 scanning electron microscope. The TSL OIM software was used for EBSD data analysis.

2.4 Three-dimensional atomic probe analysis

Samples for three-dimensional atomic probe (3DAP) analysis were machined to a thin bar with a size of 0.5 mm × 0.5 mm × 20 mm. Electro-polishing was performed in electrolyte (25 vol.% perchloric acid and 75 vol.% acetic acid) until one end of the sample became thin and sharp. The needle-tip sample was further polished by micro-electropolishing technology in a solution of 2 vol.% perchloric acid and 98 vol.% ethylene glycol butyl ether. 3DAP tests were performed on a LEAP 4000 HR analyzer at a working temperature of 50 K, a pulse speed of 200 kHz, and a pulse voltage fraction of 15%. The detection efficiency of the instrument was about 36%. We considered that more Si atoms were undetected than Mg atoms, so the average Mg/Si mass ratio of the precipitate in the experimental results was 20%−40% higher than the actual results [21], and 30% was chosen for statistical analysis. The experimental results were reconstructed and quantitatively analyzed with an IVAS 3.6.12 software, in which the maximum separation distance (D_{max}) of 0.7 nm and the minimum number of solute atoms (N_{min}) of 10 were used in the atomic clusters. In this work, the solute clusters in Al−Mg−Si alloy were separated into several groups: atomic cluster was regarded as the segregation of spherical solute atoms with less than 70 solute atoms and less than 3 nm in diameter,

whereas precipitate was considered as the segregation of solute atoms with more than 70 solute atoms. Amongst the precipitates, those with solute atom number of 70−200 and particle size of 3−6 nm were denoted as spherical-shaped precipitate (GP zone), whereas precipitates with larger particle size were referred to as needle-shaped ones.

3 Results

3.1 Artificial aging

The EBSD results show that AA alloy primarily comprises equiaxed crystals with a recrystallized microstructure (Fig. 2(a)). The average grain size is 11.43 μm, and the residual dislocation density based on the kernel average misorientation (KAM) method is 21.65×10^{12} m^{-2}. The TEM image after solid-solution heat treatment is depicted in Fig. 3(a). No strengthening phase can be detected, implying that solute atoms are dissolved into the matrix during solution treatment, and the alloy is in a supersaturated state. The microstructure of the alloy subjected to AA treatment immediately after dissolution is shown in Figs. 3(b−f). Abundant fine needle-shaped phases with an average length of 27 nm are perpendicular to one another along the $[100]_{Al}$ and $[010]_{Al}$ directions, whereas the point-shaped morphology is displayed along the $[001]_{Al}$ direction, shown as rectangles and circles in Fig. 3(b), respectively. In the corresponding $[001]_{Al}$ SADP spectrum, a clear "cross-shaped" diffraction pattern can be observed (Fig. 3(c)), indicating the presence of β'' phase. The needle-shaped phase is shown in Fig. 3(d), which is coherent with the matrix. Strain fields can be detected

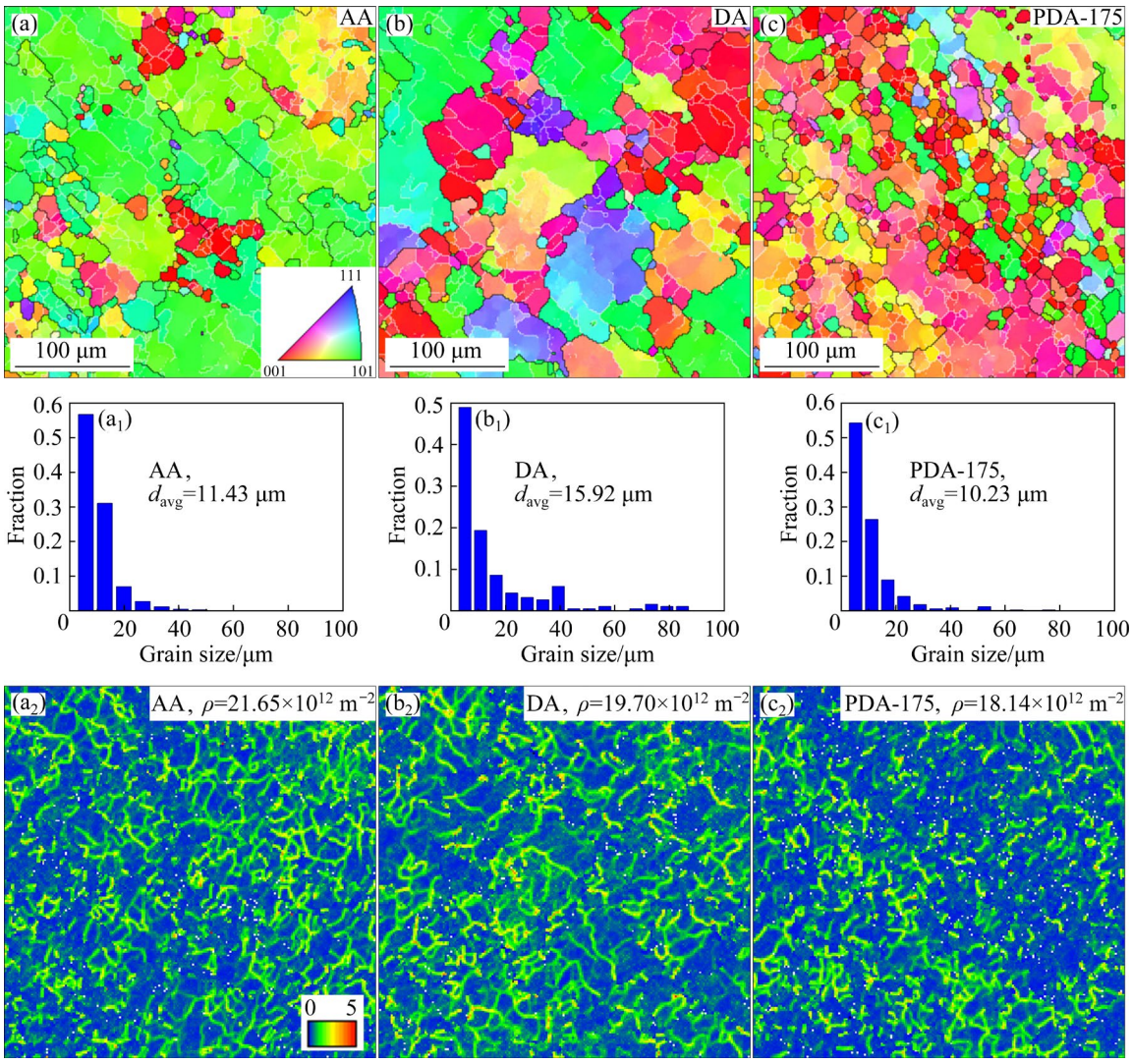

Fig. 2 EBSD analysis results of alloys: (a−c) IPF maps; (a_1−c_1) Grain size distribution; (a_2−c_2) KAM maps and dislocation density (ρ)

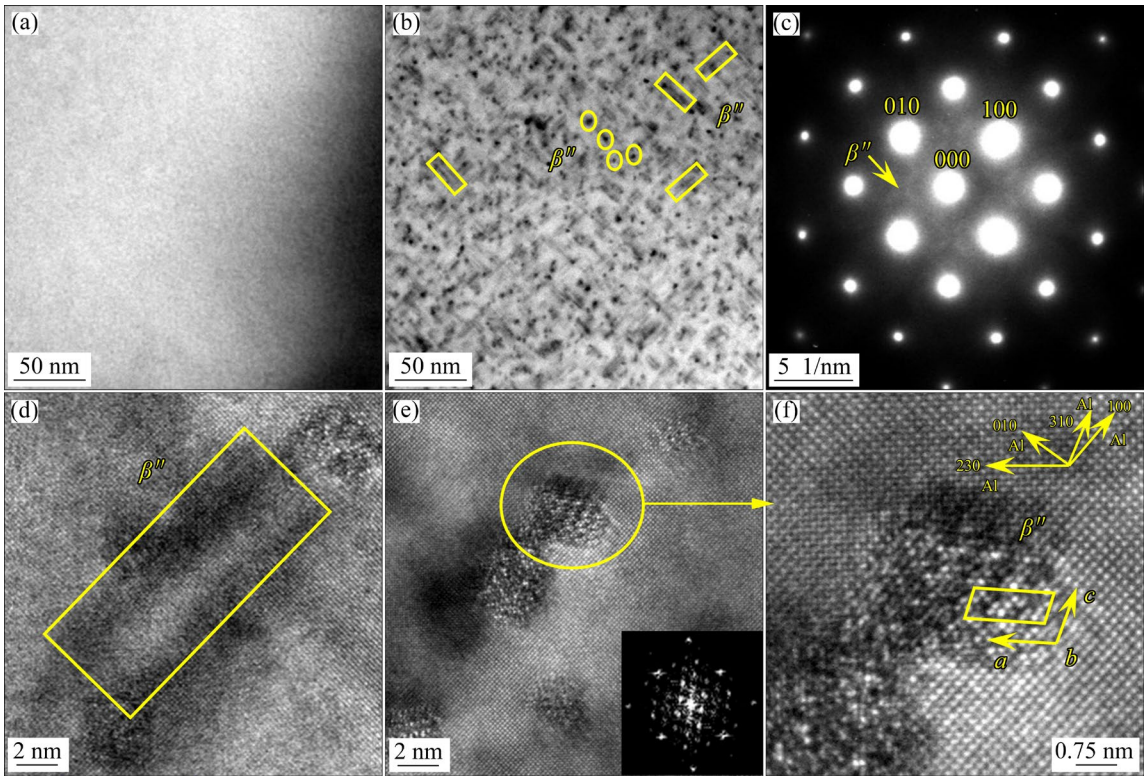

Fig. 3 Microstructure of solid-solution-treated alloy (a) and AA alloy (b−f): (b, c) TEM image and corresponding SADP image, respectively; (d−f) HRTEM images

at the boundary between the phase and the matrix. The morphology of point-shaped phase can be obtained in Fig. 3(e), which is about 4 nm in diameter and incoherent with the matrix. The related lattice parameters can be obtained with lattice constants of a=1.516 nm and c=0.674 nm, and the intersection angle β=105.26°, which can also be identified as β'' phase (Fig. 3(f)).

The high-density precipitates are uniformly distributed after AA treatment, and the average length, cross-section area, and number density of precipitates are determined for quantitative analysis, as shown in Table 2. The number density of precipitates is obtained from the formula in Ref. [20]. The strengthening β'' phase precipitates extensively from the supersaturated solid solution during AA treatment, leading to the hardness increasing from HV (54.1±1.2) in supersaturated state to HV (130.9±1.0) of the AA alloy, whereas the yield strength (YS) and ultimate tensile strength (UTS) increase from (210±2) and (231±3) MPa to (369±5) and (397±3) MPa, respectively. Elongation (EL) decreases from (18.8±0.4)% to (16.8±0.6)%, as shown in Table 3.

Table 2 Precipitate morphology parameters of different alloys

Alloy	Average length/nm	Average cross-section area/10^{-18}m^2	Number density/10^{23}m^{-3}	Volume fraction/%
AA	27	4.5	5.6	0.68
DA	51	7.1	1.4	0.50
PDA-100	25	5.3	4.0	0.55
PDA-175	29	5.3	4.3	0.66

Table 3 Hardness and tensile properties of different alloys

Alloy	Hardness (HV)	YS/MPa	UTS/MPa	EL/%
Solid-solution	54.1±1.2	210±2	231±3	18.8±0.4
AA	130.9±1.0	369±5	397±3	16.8±0.6
NA	76.9±0.8	280±6	296±5	20.6±0.8
DA	106.3±1.9	305±6	322±6	12.4±1.3
PN-100	70.2±1.6	–	–	–
PN-175	102.2±3.8	320±3	338±5	18.0±0.4
PDA-100	117.9±3.5	350±4	370±3	14.6±0.4
PDA-175	124.5±1.9	376±4	393±2	13.5±0.7

3.2 Natural aging

The TEM images after NA treatment of the alloy are presented in Fig. 4. No conspicuous precipitate can be detected in the matrix. The atomic arrangement observed from the HRTEM image is well organized with a coherent structure, implying that no precipitate is generated from the matrix. The corresponding inverse fast Fourier transform (IFFT) pattern is presented in Fig. 4(c). Solute cluster is fully coherent within the matrix, and no lattice distortion occurs during NA treatment.

Furthermore, 3DAP analysis was used to identify the solute clusters of the NA alloy. Figure 5(a) demonstrates that a large number of spherical atomic clusters form after NA treatment. The distribution positions of Mg atoms and Si atoms are highly coincident, implying that Mg atom, Si atom, and nearby Al atom are segregated to form Mg−Si atomic clusters. No segregation of other solute elements can be detected.

The arrangement of solute atoms is analyzed by the nearest neighbor distance (NND) method as shown in Figs. 5(b, c). From the actual and random distribution curves of solute atoms, Mg and Si atoms are non-randomly distributed in the matrix, and the actual solute atom spacing decreases compared with that of the random distribution, in which the deviation distances of Mg and Si atoms are 0.26 and 0.24 nm, respectively. The high coincidence of the actual distribution of Mg and Si atoms can also indicate the formation of Mg−Si atomic clusters.

The statistical results of the solute clusters from 3DAP analysis are shown in Figs. 5(d, e) and Table 4. Only atomic clusters are detected in the NA alloy, the number density of the cluster is 1.22×10^{23} m^{-3}, and each cluster contains 24 solute

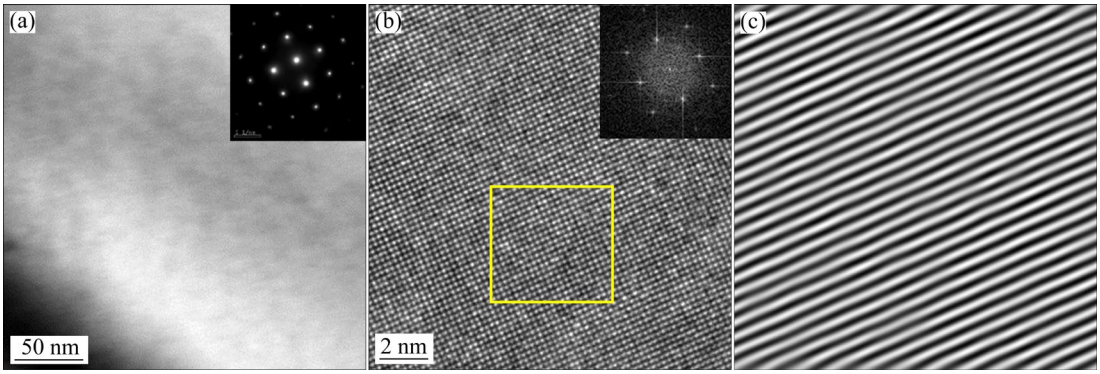

Fig. 4 Microstructure of NA alloy: (a) TEM image; (b) HRTEM image; (c) IFFT pattern corresponding to yellow box in (b)

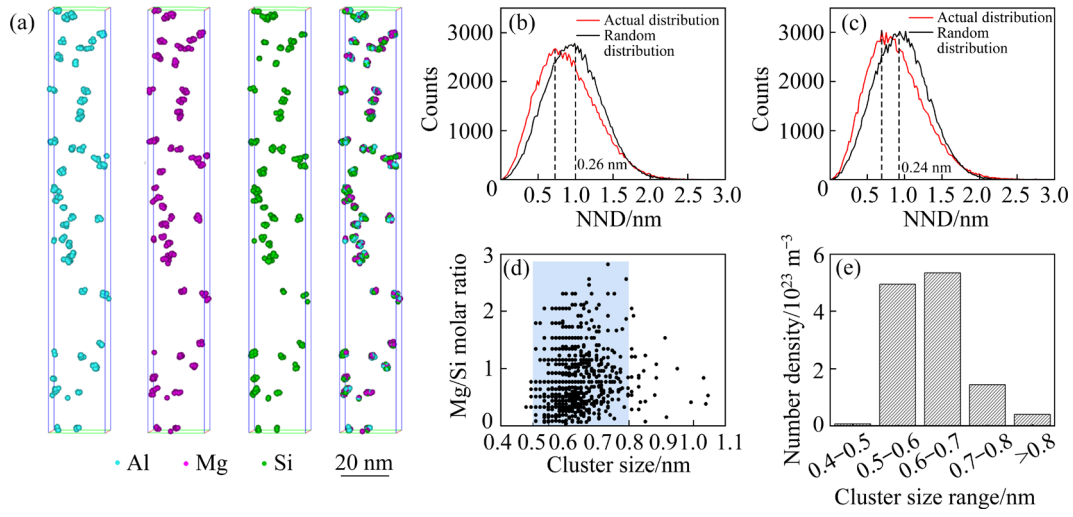

Fig. 5 (a) 3D distribution of Al, Mg and Si solute atoms, and Mg−Si clusters of NA alloy; (b, c) Nearest neighbor atom distribution of Mg and Si atoms, respectively; (d, e) Relationships between cluster size and Mg/Si molar ratio, and between cluster size range and number density

Table 4 3DAP statistical data of NA and PN alloys

Alloy	Equivalent radius/nm	Number density of clusters/ 10^{23} m^{-3}	Number density of precipitates/ 10^{23} m^{-3}	Average Mg/Si molar ratio
NA	0.63	1.22	−	0.85
PN-175	0.89	8.78	2.96	1.10

atoms on average. During NA treatment, solute atoms gather to form Mg−Si atomic clusters through diffusion. The Mg/Si molar ratio of atomic clusters formed during NA treatment is relatively dispersed but primarily concentrated within the range of 0.2−2 with an average Mg/Si molar ratio of 0.85. The size of atomic clusters is normally distributed and primarily concentrated within the range of 0.5−0.8 nm, whereas the number of atomic clusters with size exceeding 0.9 nm is very small. The average cluster radius is 0.63 nm, indicating relatively small size of atomic clusters, and no precipitate exists in the matrix during NA treatment. Generally, small clusters are unstable and easy to dissolve into the matrix. Due to the coherent structure and the very close atomic radius of Al, Mg, and Si atoms, the lattice distortion caused by solute clustering is slight. The atomic clusters cannot show obvious strain field contrast, and detecting the atomic cluster signal in TEM observation is difficult.

The strengthening effect of atomic cluster is obvious, and the hardness of NA alloy increases rapidly with the increase of NA time at the beginning, followed by a slow increase, as shown in Fig. 6. The hardness value increases to HV (76.9±0.8) after NA for 48 h, which is 42.1% higher than that of the solid-solution alloy. Similarly, the YS and UTS increase to (280±6) and (296±5) MPa after NA treatment, respectively, as shown in Table 3.

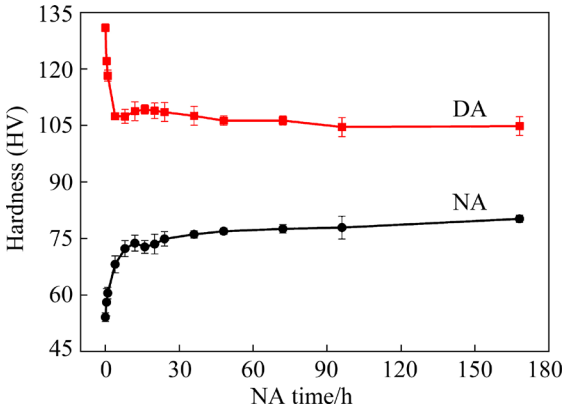

Fig. 6 Variation in hardness of NA and DA alloys with NA time

3.3 Delayed aging

The microstructure of DA alloy is shown in Fig. 2(b) and Fig. 7. Low-density, coarse elongated phases exist obviously in the matrix (Fig. 7(a)). HRTEM analysis reveals that strengthening phases β'' and β' coexist in the matrix, with the β'' phase being predominant. Statistical analysis shows that the average length of these phases is about 51 nm,

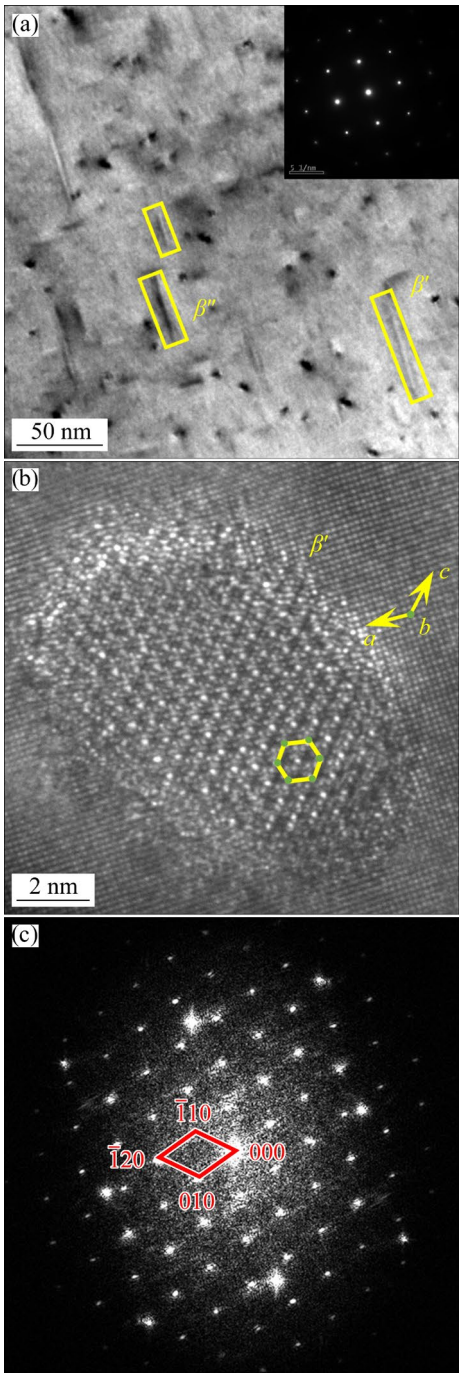

Fig. 7 Microstructures of DA alloy: (a) TEM image; (b) HRTEM image; (c) FFT image

and the number density is 1.4×10^{23} m^{-3}. Figures 7(b, c) present the HRTEM and the corresponding FFT image of a point-shaped precipitate, respectively, which can be identified as β' phase by measuring the related lattice parameters a=0.715 nm and intersection angle γ=120°. The strengthening ability of β' phase is weaker than that of β'' phase [8]. Compared with that of AA alloy, the phase size of DA alloy increases significantly, whereas the number density decreases obviously, as shown in Table 2. Correspondingly, the mechanical properties of DA alloy decrease distinctly. Table 3 shows that the hardness of DA alloy is 81.2% that of AA alloy, whereas the YS, UTS, and EL are 82.7%, 81.1%, and 73.8% those of the AA alloy, respectively. Additionally, the hardness of the DA alloy decreases rapidly with the increase of NA time at the beginning before roughly remaining constant, as presented in Fig. 6. NA occurs during DA treatment, leading to the formation of Mg−Si atomic clusters in the matrix. These atomic clusters affect the precipitation of strengthening phases during subsequent AA treatment, resulting in significantly reduced hardness and tensile properties.

3.4 Pre-aging before natural aging

The TEM images of PN alloy after PA treatment at 100 and 175 °C are shown in Fig. 8. No obvious precipitates can be observed in PN-100 alloy (Fig. 8(a)), but a small amount of spherical-shaped GP zone can be detected from the HRTEM image (marked with yellow square box). The GP zone signal can be found in the corresponding fast Fourier transform (FFT) pattern (Fig. 8(b)). The GP zone comprises Mg and Si atoms in addition to Al atoms, showing coherence with the matrix. Due to the small difference in atom radius amongst Mg, Si, and Al atoms, the lattice distortion caused by the formation of GP zone is not obvious. In the corresponding IFFT pattern shown in Fig. 8(c), no significant lattice distortion can be observed, only slight distortion can be detected as marked with an arrow, implying that the GP zone is coherent with the matrix. In addition to GP zone, atomic clusters are also present in the PN-100 alloy.

As the PA temperature reaches 175 °C, abundant precipitated phases are uniformly distributed along the $[001]_{Al}$ direction (Fig. 8(d)). The radius of the phase is about 2 nm with a disordered structure, which can be regarded as the

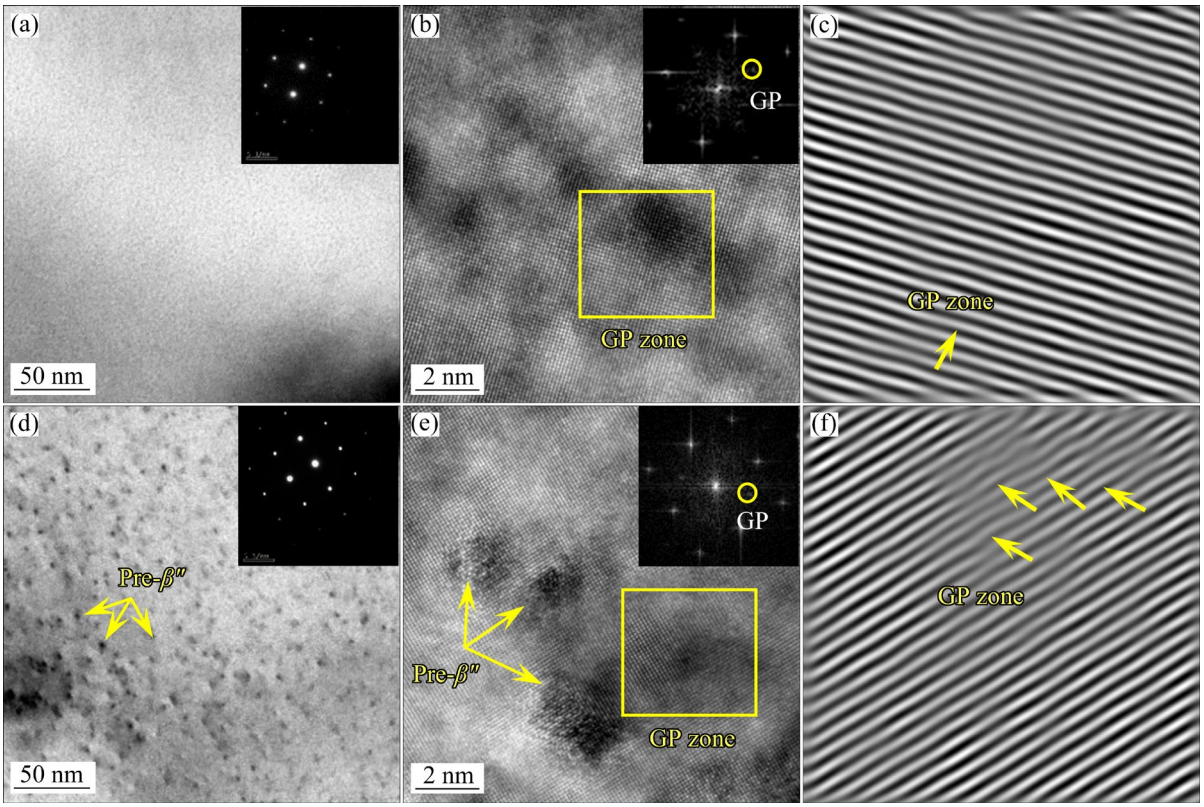

Fig. 8 Microstructures of PN alloys after PA treatment at 100 °C for 0.5 h (a−c) and 175 °C for 0.5 h (d−f): (a, d) TEM images; (b, e) HRTEM images; (c, f) IFFT patterns

pre-β'' phase [29]. The pre-β'' phase is considered as the nucleus of the β'' phase. The signal of needle-shaped phase along $[100]_{Al}$ and $[010]_{Al}$ directions is relatively weak in PN-175 alloy, meaning that the pre-β'' phase is small. Except for the needle-shaped phase, GP zones can also be detected from the HRTEM image, and the GP zone signal in the corresponding FFT is obvious. In the corresponding IFFT pattern as depicted in Fig. 8(f), GP zone can be easily detected with obvious lattice distortion, as marked with arrows, implying severe solute clustering.

The detailed atomic arrangement information of PN-175 alloy according to 3DAP analysis is shown in Fig. 9(a). Mg and Si atoms are segregated strongly with Al atoms. Long strips of solute clusters can be obtained, and the morphology varies with the direction of precipitation. Needle shape is found in the length direction and nearly round shape in the cross-sectional direction. Additionally, a number of fine spherical precipitates can be detected, similar to the morphology of the NA alloy shown in Fig. 5(a) and can be considered as Mg−Si atomic clusters. Moreover, GP zone is also present in the matrix due to the TEM observation and the precipitation sequence with size intermediate between cluster and precipitate.

According to the NND curve of solute atoms of PN-175 alloy (Figs. 9(b, c)), the segregation distance of Mg and Si atoms increases to 0.44 nm, implying that solute atom segregation is enhanced after PA treatment compared with NA alloy (Figs. 5(b, c)). In this state, the small spherical-shaped solute clustering can be referred to as Mg−Si atomic clusters and GP zone, whereas the large needle-shaped precipitate represents pre-β'' phase. Mg−Si atomic cluster, GP zone, and pre-β'' phase can be detected after PA treatment according to the combined analysis of TEM and 3DAP, dominated by cluster and GP zone. The radius of GP zone is about 2 nm, and the size of needle-shaped precipitates is about 15 nm × 5 nm × 5 nm. The corresponding statistical results of solute clusters are shown in Table 4. Each solute cluster in PN-175 alloy contains 136 solute atoms on average, and the equivalent radius increases to 0.89 nm. The number density of atomic cluster and precipitate is 8.78×10^{23} and 2.96×10^{23} m^{-3}, respectively. Therefore, the size and number density of Mg−Si solute clusters of PN alloy obviously increase compared with the atomic arrangement of NA alloy (Fig. 5), leading to the increased hardness from HV (76.9±0.8) of NA alloy to HV (102.2±3.8) of PN-175 alloy. Besides, due to the large presence of GP zone and pre-β'' phase (Fig. 8(d)), the hardness of PN-175 alloy is much higher than that of PN-100 alloy.

The size distribution of solute clusters of PN-175 alloy is depicted in Figs. 9(d, e). Compared with NA alloy, the size distribution of the precipitates is relatively dispersed but concentrated in the region of 0.5−0.9 nm, as marked with a blue box. The number of atomic clusters and precipitates larger than 0.9 nm increases significantly (marked

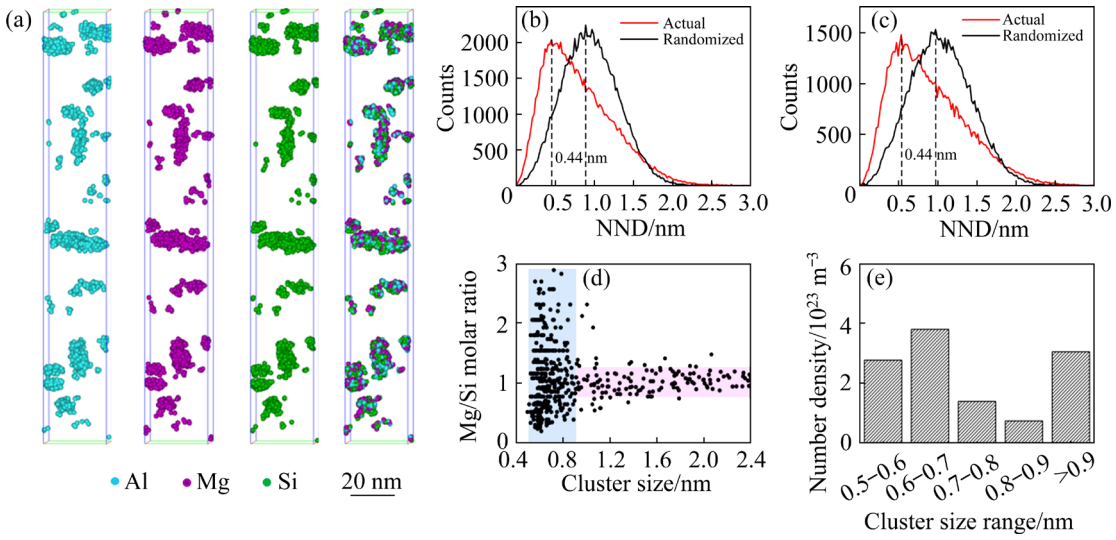

Fig. 9 (a) 3D distribution of Al, Mg and Si solute atoms, and Mg−Si clusters of PN-175 alloy; (b, c) Nearest neighbor atom distribution of Mg and Si atoms, respectively; (d, e) Relationships between cluster size and Mg/Si molar ratio, and between cluster size range and number density

with a pink box). The average Mg/Si molar ratio of solute clusters is 1.10, in which the Mg/Si molar ratio of small clusters with size between 0.5 and 0.9 nm is relatively dispersed, whereas the Mg/Si molar ratio of solute clusters with size larger than 0.9 nm is concentrated between 0.8−1.2. Compared with the statistical results of NA alloy (Figs. 5(d, e)), a great number of precipitates with larger size appear, and the average Mg/Si molar ratio, number density, and equivalent radius of solute clusters increase obviously after PA treatment (Table 4), indicating the formation of numerous atomic clusters and precipitates with large size during PA treatment.

With the aid of PA, the hardness of PN alloy hardly changes with the increase of the NA time, as shown in Figs. 10(a, b). The hardness of PN-100 alloy immediately after PA treatment is HV (72.5±0.4), which then increases to HV (73.1±2.1) after NA for 168 h. Meanwhile, the initial hardness of PN-175 alloy is HV (99.9±2.3) and then changes to HV (102.2±2.5), implying that the solute clusters formed during PA are stable and do not change during the NA process.

3.5 Delayed aging after pre-aging

The microstructure of PDA alloy is shown in Fig. 2(c) and Fig. 11. Abundant nanoscale β'' phases are evenly distributed. The length of β'' phase in PDA alloy is about 30 nm, and the number density of β'' phase is close to that of AA alloy (Fig. 3(b)), which largely differs from that of DA alloy (Fig. 7). The morphology and distribution of the precipitates in PDA alloy are beneficial to strengthening ability, resulting in the improved strength and hardness of the alloy. According to 3DAP and HRTEM analyses, stable atomic clusters and fine precipitates are produced during PN treatment, consuming solute atoms and quenching vacancies, thus leading to decreased supersaturation of solute elements and vacancies. The formation of small atomic clusters is prevented when the alloy is parked at room temperature, ultimately improving the mechanical properties. The hardness of PDA-175 alloy is 95.1% that of AA alloy, whereas the YS, UTS, and elongation are 101.9%, 99.0%, and 80.4% those of AA alloy, respectively, as shown in Figs. 10(c, d) and Table 3. The hardness and strength of PDA-175 alloy are close to those of AA alloy.

Additionally, compared with the microstructure of PDA alloy after PA at 100 and 175 °C, the precipitate size and the number density of the latter alloy is slightly larger. The average length

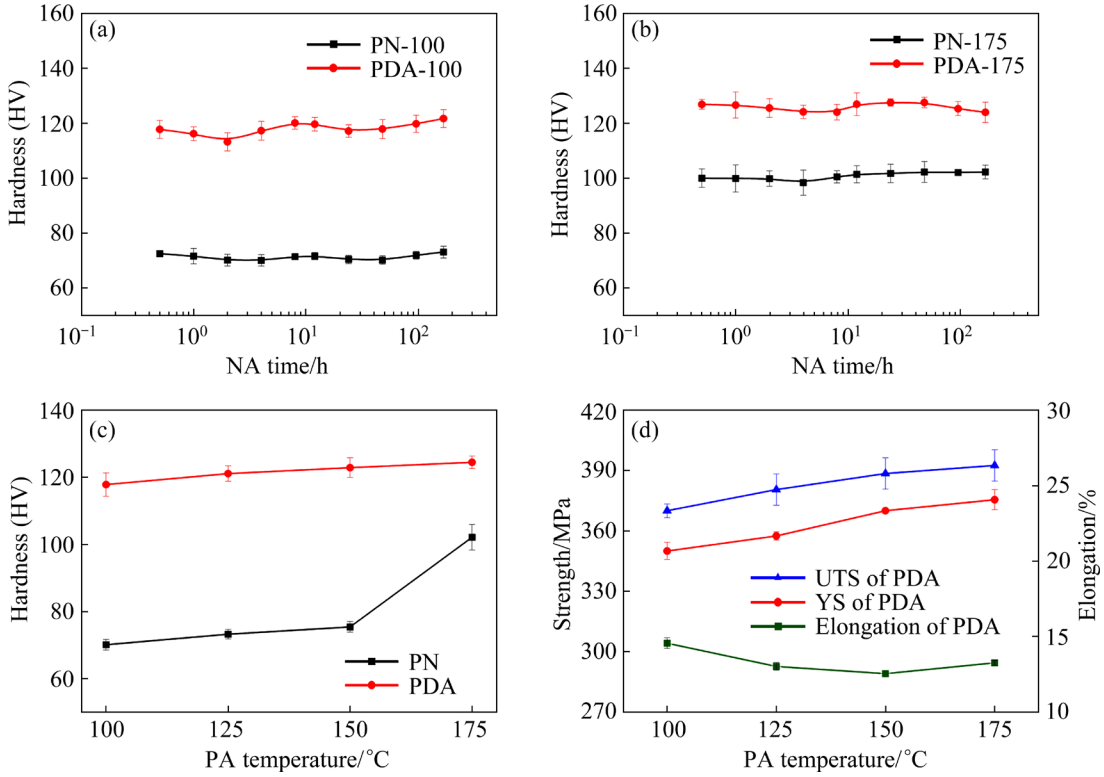

Fig. 10 (a, b) Variation in hardness with NA time for PN and PDA alloys at PA temperatures of 100 and 175 °C, respectively; (c, d) Variation in hardness and tensile mechanical properties with PA temperature, respectively

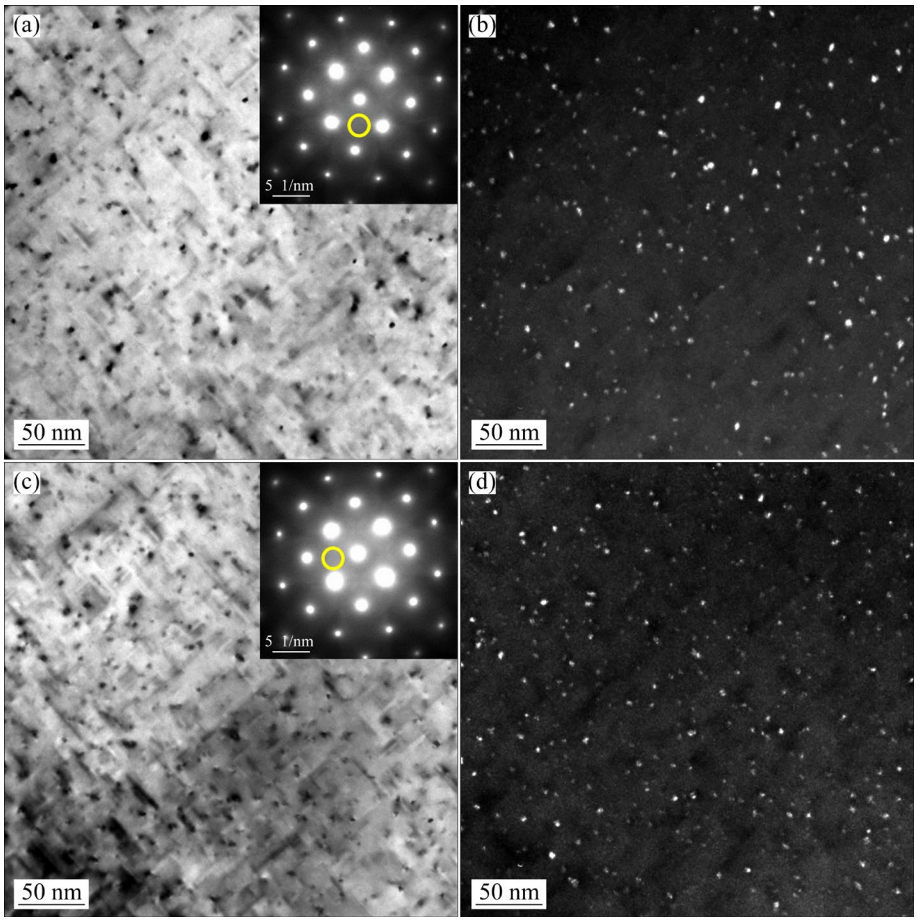

Fig. 11 Bright-field (a, c) and dark-field (b, d) TEM images of PDA alloys: (a, b) PDA-100; (c, d) PDA-175

and the number density of β'' phase in PDA-175 alloy are close to those of AA alloy and higher than those of PDA-100 alloy (Table 2), resulting in a better strengthening effect of PDA-175 alloy. Besides, the variation of mechanical properties of PDA alloy shows that the hardness and strength increase with the PA temperature changes from 100 to 175 °C (Figs. 10(c, d)), indicating that the optimized PA temperature in the studied alloy is 175 °C.

4 Discussion

4.1 Effect of Mg−Si segregation morphology on strengthening ability

Several strengthening mechanisms operate together in the heat-treated alloys. The total contribution to the YS is the linear accumulation of individual strengths, including solid-solution strengthening, grain-boundary strengthening, dislocation strengthening, and precipitation strengthening [8]. The macroscopic YS (σ) of the alloy can be written as follows:

$$\sigma=\sigma_0+\sigma_{ss}+\sigma_{gb}+\sigma_d+\sigma_p \quad (1)$$

where σ_0 is the intrinsic strength of pure Al being 10 MPa, and σ_{ss}, σ_{gb}, σ_d, and σ_p are the strengths due to the solid solution, grain boundary, dislocation, and precipitation, respectively. Solid-solution strengthening is related to the nature of the solute atom and the average solute concentration. Given that the alloys have the same chemical composition and experience identical final AA treatment, the difference of the solution element contents in the matrix is very small. It can be assumed that the difference in σ_{ss} on the strength is negligible, and the contribution of solid-solution strengthening is considered to be 15 MPa.

The strength caused by grain boundary is negatively correlated with grain size, which can be derived from the Hall−Petch equation [30]:

$$\sigma_{gb}=\sigma_a+kd^{-1/2} \quad (2)$$

where σ_a and k are coefficients with values of 19.2 MPa and 0.17 MPa·m$^{0.5}$, respectively, and d is the average grain size, as obtained from the EBSD

data (Fig. 2).

Strength referring to dislocation (σ_d) is usually assumed to be related to dislocation density. It can be obtained from the Bailey–Hirsch equation [31]:

$$\sigma_d = M\alpha_d Gb\sqrt{\rho} \tag{3}$$

where M(=3.06) is the average matrix orientation factor of Al, α_d(=0.2) denotes the material correlation constant, b and G represent the magnitude of Burgers vector and the shear modulus of the matrix, respectively, and ρ stands for dislocation density, which is expressed using the residual dislocation density in EBSD analysis (Fig. 2).

For Al−Mg−Si alloy, precipitation strengthening is considered to be an effective strengthening method [32]. Nanosized phases precipitate from the matrix during the aging treatment, which act as pinning points to hinder dislocation movement. The strain field caused by the precipitates also produces a barrier to the dislocation movement. The interaction between precipitated phases and dislocations results in the strengthening effect of the alloy. The β'', pre-β'', GP zone, and atomic clusters are assumed to be dislocation shearable. The obstacle strength (F) referring to dislocation shearable precipitate is expressed as [33]

$$F = 2\delta Gb^2(r/r_c) \tag{4}$$

where r is the radius of the precipitate or cluster, r_c is the transition radius between precipitation shearing and bypassing, and δ (=0.5) is a geometric constant. Then, the precipitation strength (σ_p) induced by the cutting mechanism can be derived as [34]

$$\sigma_p = \frac{NF^{3/2}}{b^2\sqrt{\delta G}}\sqrt{N_v r} \tag{5}$$

where N (=3) is the average polycrystal Taylor factor, and N_v is the number density of the precipitates or clusters. Notably, the precipitation strength of NA alloy is solely provided by atomic clusters, whereas alloys that experience AA treatment (e.g., AA, DA, and PDA alloys) comprise needle-shaped precipitates. The precipitation strength primarily depends on these precipitates. For PN alloy comprising clusters and precipitates, precipitation strength can be refined according to $\sigma_p = \sqrt{\sigma_{cl}^2 + \sigma_{ppt}^2}$ [34], where σ_{cl} and σ_{ppt} are the strength contributions of the clusters and needle-shaped precipitates, respectively, and can be obtained from Eq. (5).

For DA alloy, β'' and β' precipitates coexist in the matrix. Different from β'' precipitate, β' precipitate serves as an obstacle where dislocation motion proceeds by bypassing. The obstacle strength F referring to dislocation bypass precipitate is constant, as shown in Eq. (6). Precipitation strength σ_p according to the bypassing mechanism can be expressed in Eq. (7) [33]:

$$F = 2\delta Gb^2 \tag{6}$$

$$\sigma_p = \sqrt{\frac{6}{\pi}}\frac{N\delta Gb}{1.15}\frac{\sqrt{f_v}}{r} \tag{7}$$

where f_v is the volume fraction of the precipitates.

Based on the data derived from 3DAP, TEM, and EBSD results, the final calculation results of the strengthening contribution are determined and shown in Fig. 12. The calculated strengths are close to experimental values. Notably, the strength calculations do not consider the dispersion strengthening effect of the AlMnFeSi phase. AlMnFeSi phase is always present in the alloy and contributes to the strength by hindering the movement of dislocations. Assuming that AlMnFeSi phase has an average size of 100 nm and a volume fraction of 0.15%, respectively, it induces a strength increment of 12 MPa through bypass mechanism [20]. Thus, combined with the dispersion strengthening capability, the strength calculation results well agree with the experimental values. For alloys that experience AA treatment, the precipitation strengthening contributes the most amongst these strengthening mechanisms, accounting for 67.0%, 63.2%, and 67.4% strength

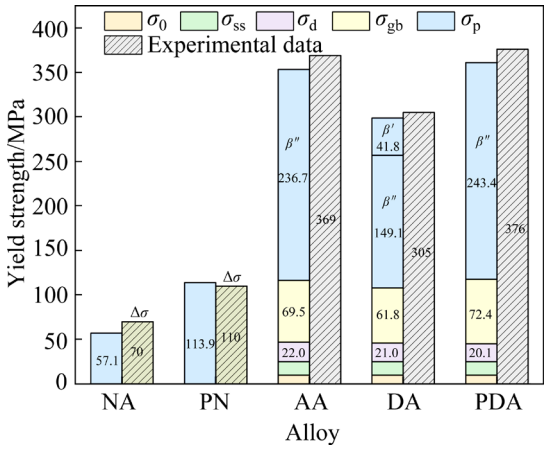

Fig. 12 Strengthening contributions of different alloys

for AA, DA, and PDA alloys, respectively. For alloys subjected to NA and PN treatment, the increase in strength compared with solid solution alloy ($\Delta\sigma$) is attributed to precipitation strengthening because the value of precipitation strengthening is close to the increment of strength. Additionally, the strengthening ability of PN alloy is much higher than that of NA alloy, which is attributed to the stronger precipitation strengthening of clusters and pre-β'' phases with large size and high number density in PN alloy.

4.2 Effect of aging treatments on microstructure evolution

4.2.1 Effect of delayed aging

Excessive vacancies are produced after high-temperature solution and quick quenching, and the high solute atom−vacancy binding energy favors the formation of atom−vacancy pairs during NA, followed by the generation of atomic clusters. Atomic clusters play a significant role in microstructure evolution during subsequent AA, thereby influencing the strengthening ability. During NA, numerous Mg−Si clusters are formed, and the cluster size is concentrated within the range of 0.5−0.8 nm. The Mg/Si molar ratio is relatively dispersed with an average Mg/Si molar ratio of 0.85, as shown in Fig. 5(d). For atomic clusters with various sizes according to Ostwald ripening theory [35], smaller atomic clusters are unstable and easily redissolve back into the matrix during subsequent AA. Thus, they cannot be used as stable nucleation sites for strengthening precipitation, resulting in the reduction of effective nucleation number. Conversely, the larger ones are more stable and can serve as precipitation nucleation sites or directly transform into strengthening precipitation. In this case, the number of nucleation sites in DA alloy is limited, thereby affecting the density and distribution of subsequent precipitation. Consequently, the mechanical properties deteriorate.

Additionally, due to the generation of atomic clusters and the re-dissolution of the small clusters, quenching vacancies are mostly occupied during NA, and the equilibrium vacancy concentration can be reached. The precipitation kinetics is lower than that in the non-delayed state [36]. The decrease in quenching vacancy concentration reduces the diffusion rate of solute atoms, lowering the formation of new strengthening precipitates during subsequent AA treatment. The solute atoms prefer to precipitate on the large cluster-nucleation site formed during NA, leading to the rapid growth of the precipitate. Accordingly, low density and coarse β'' and β' precipitates can be obtained through the preferential growth and coarsening of larger size clusters after DA treatment (Fig. 7).

The microstructure evolution of DA alloy is shown in Fig. 13. High solute supersaturation and numerous excess vacancies are obtained after quenching. Vacancies accelerate the diffusion of solute atoms and provide favorable nucleation sites for cluster formation. Small clusters with low Mg/Si molar ratio are produced after NA (marked with red box), reducing the supersaturation of solute atoms and occupying the quenching vacancies. In subsequent AA treatment, the decreased diffusion rate of solute atoms and the limited nucleation site number of the precipitates lead to reduced number density of the precipitates. Furthermore, the solute atoms in the matrix preferentially precipitate at the existing nucleation

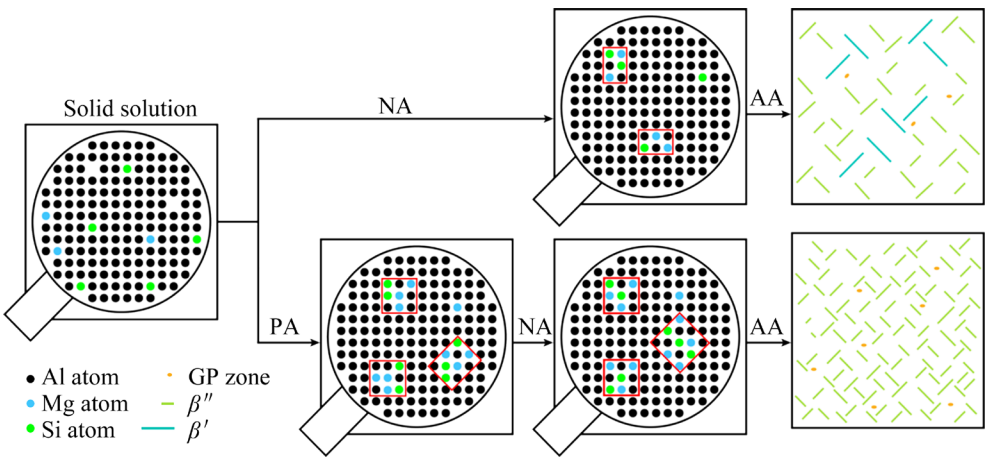

Fig. 13 Schematic diagram of microstructure evolution of DA and PDA alloys

sites, resulting in rapid coarsening of the precipitates. Thus, the strengthening β'' phase becomes coarse, and a number of β'' phases transform into β' phases. Therefore, coarse β'' and β' phases are present after DA treatment, where β'' phase is dominant. The number density of the precipitate is 1.4×10^{23} m^{-3}, which is lower than that of AA alloy, and the average size of the precipitates is 51 nm, which is far larger than that of AA alloy (Fig. 7, Fig. 3(b), and Table 2). The coarsening of β'' and β' phases and the reduced precipitate number density result in the significantly reduced precipitation strength. As shown in Fig. 12, the precipitation strengthening contribution decreases from 236.7 MPa in AA treatment to 190.9 MPa in DA treatment, which is the main reason for the decrease in strength of DA alloy.

4.2.2 Effect of pre-aging

Mg−Si atomic cluster, GP zone, and pre-β'' phase are produced in the PN-175 alloy, the size range of solute clusters is within 0.5–2.4 nm. Compared with NA treatment, the equivalent radius and the number density of atomic clusters increase from 0.63 to 0.89 nm and from 1.22×10^{23} to 8.78×10^{23} m^{-3}, respectively, but the number of atomic clusters with 0.5−0.7 nm in size is reduced. Conversely, there exist a large number of solute clusters with sizes larger than 0.9 nm, accompanied by the appearance of GP zone and pre-β'' phase (Fig. 8(d) and Fig. 9). Thus, the number of small and unstable atomic clusters is reduced, whereas larger and more stable solute clusters are produced substantially during short-time high-temperature PA treatment. Besides, the Mg/Si molar ratio of PN alloy is also relatively concentrated, especially for solute clusters with sizes larger than 0.9 nm (Fig. 9(d)), which is primarily concentrated in the region of 0.8−1.2 with an average of 1.10 and is higher than that of NA alloy. The solute cluster generated in PA treatment is chemically and morphologically similar to the precipitate produced at the initial stage of AA treatment and more structurally stable than those formed in NA treatment. The increase in Mg/Si molar ratio may be due to the reduced difference in diffusion coefficient between Mg and Si atoms and the increased diffusivity of Mg atoms at high temperatures. According to the diffusion theory, the diffusion coefficient (D) can be expressed by the Arrhenius equation:

$$D=D_0\exp[-Q/(RT)] \tag{8}$$

where D_0 is the self-diffusion coefficient, Q is the diffusion activation energy, which are material-related parameters, R is the molar gas constant, and T is the thermodynamic temperature. The diffusion coefficients of Mg and Si atoms at the studied temperatures are calculated, as shown in Table 5. Compared with the Mg atom at room temperature (20 °C), the diffusion coefficient of Si is much higher. The difference in diffusion coefficient decreases at a PA temperature of 175 °C, implying that more Mg atoms can diffuse into atom clusters at elevated temperatures, thus increasing the Mg/Si molar ratio of the cluster segregations.

4.2.3 Effect of pre-aging on delayed aging

After PN treatment, atomic clusters and GP zones with high molar Mg/Si ratio are preferentially precipitated in the alloy. Unlike the atomic clusters formed during NA treatment, these large solute clusters formed after PA treatment are relatively stable, showing different precipitation effects during subsequent aging treatment. On the one hand, the large solute clusters consume numerous solute atoms and lower the solute concentration, leading to reduced atom-cluster formation during NA treatment. On the other hand, the solute clusters formed during PN treatment occupy quenching vacancies, thereby decreasing the vacancy concentration. The formed solute clusters decrease the nucleation driving force and the potential for new atomic clustering. The PN treatment effectively prevents the precipitation of small atomic clusters at room temperature and mitigates the NA negative effects, as evidenced by the stability of hardness with increased NA time (Figs. 10(a, b)).

Besides, due to the larger size, higher Mg/Si molar ratio, and relatively stable structure of the

Table 5 Diffusion coefficients of Mg and Si atoms at different temperatures

Atom	D_0/(m^2·s^{-1}) [37]	Q/(kJ·mol^{-1}) [37]	D_{NA} (20 °C)/(kJ·mol^{-1})	D_{PN} (175 °C)/(kJ·mol^{-1})
Mg	1.49×10^{-5}	120500	4.90057×10^{-27}	1.32727×10^{-19}
Si	1.38×10^{-5}	117600	1.49264×10^{-26}	2.67788×10^{-19}

solute clusters formed during PN treatment (Table 4), the precipitate of the strengthening phase during AA treatment is promoted. The solute clusters do not easily redissolve back into the matrix in AA treatment, so more precipitation nucleation sites can be retained. Owing to the increase in precipitation nucleation sites and slow growth rate, these atomic clusters and GP zones finally transform into fine β'' phase during subsequent aging, improving the strengthening ability of the alloy. Therefore, with the aid of short-time high-temperature PA treatment, the microstructure of PDA alloy can be reasonably adjusted and controlled, high density and fine β'' phases uniformly precipitate, and the alloy strengthening effect is improved compared with that of DA alloy with the increased precipitation strength from 190.9 to 243.4 MPa (Fig. 12). The strength and hardness of PDA alloy approximately reaches the levels of AA alloy, effectively avoiding the strength loss caused by the NA negative effect at room temperature and improving the strengthening ability of DA alloy.

The schematic diagram of microstructure evolution of PDA alloy is shown in Fig. 13. Large atomic clusters and GP zone with high Mg/Si molar ratio are produced during short-time PA treatment (marked with red box), consuming the solute atoms and occupying the quenching vacancies greatly in the matrix, leading to the prevention of small atomic cluster precipitation when parked at room temperature. Additionally, the clusters and GP zones that precipitate during PA treatment are more stable. Except for a small amount of these clusters dissolving back into the matrix, most of them can serve as nucleation cores for the generation of strengthening phase during the subsequent AA treatment. Due to the large number of nucleation sites, numerous fine β'' precipitates are formed. The number density and size of the precipitates in PDA alloy are similar to those in AA alloy. The variation in microstructure leads to improved mechanical properties of PDA alloy, and the strengthening ability of the alloy is restored after NA at room temperature.

5 Conclusions

(1) Atomic clusters with an average size of 0.63 nm and a Mg/Si molar ratio of 0.85 are formed during NA treatment. They are unstable, forming low-density and coarse β'' and β' phases during the subsequent AA treatment, leading to the reduced strengthening capacity of DA alloy.

(2) Atomic clusters and GP zones with an average size of 0.89 nm and a concentrated Mg/Si molar ratio of 1.10 are produced during PN-175 treatment, which can prevent the generation of small clusters during NA treatment. They can serve as effective nucleation sites for strengthening precipitation during AA treatment, thereby enhancing the strengthening ability of PDA alloy.

(3) Compared with AA treatment, DA treatment plays a negative role in strengthening ability. With the aid of short-time PA at 175 °C before DA treatment, the strengthening ability is recovered, implying that the NA negative effect of Al−Mg−Si alloy can be mitigated through PA treatment at elevated temperatures.

(4) Grain boundary strengthening, dislocation strengthening, and precipitation strengthening capabilities of alloys in various aging states are calculated. The results well agree with the experimental values.

CRediT authorship contribution statement

Shu-hui LIU: Funding acquisition, Investigation, Writing – Original draft; **Qing-lin PAN:** Conceptualization, Methodology; **Hong-feng HUANG:** Resources; **Jing WANG:** Supervision; **De-gui LI:** Validation; **Zhi-xin NING:** Investigation; **Li-li WEI:** Funding acquisition, Writing – Review & editing.

Declaration of competing interest

The authors declare that they have no known competing financial interests or personal relationships that could have appeared to influence the work reported in this paper.

Acknowledgments

This work was supported by the National Natural Science Foundation of China (No.52261007), the Science and Technology Project of Guangxi, China (No. GKAD22035039), and the Opening Fund for Key Laboratory of New Processing Technology for Nonferrous Metal & Materials, Ministry of Education, Guilin University of Technology, China (Nos. 22KF-11, 22KF-14).

References

[1] XU Xue-hong, ZHU Wen-bo, GUO Xiao-bin, LIANG

Chao-jie, DENG Yun-lai. Effect of aging treatment process on the microstructure development and mechanical properties of 6082 Al alloy [J]. Journal of Alloys and Compounds, 2023, 935: 167892.

[2] PEDERSEN K O, LADEMO O G, BERSTAD T, FURU T, HOPPERSTAD O S. Influence of texture and grain structure on strain localisation and formability for AlMgSi alloys [J]. Journal of Materials Processing Technology, 2008, 200: 77−93.

[3] WENG Yao-yao, JIA Zhi-hong, DING Li-peng, LIAO Jin, ZHANG Ping-ping, XU Ya-qi, LIU Qing. Effect of pre-straining on structure and formation mechanism of precipitates in Al−Mg−Si−Cu alloy [J]. Transactions of Nonferrous Metals Society of China, 2022, 32: 436−447.

[4] YANG Ming-jun, OREKHOV A, HU Zhi-yi, FENG Man, JIN Shen-bao, SHA Gang, LI Kai, SAMAEE V, SONG Min, DU Yong, van TENDELOO G V, SCHRYVERS D. Shearing and rotation of β'' and β' precipitates in an Al−Mg−Si alloy under tensile deformation: In-situ and ex-situ studies [J]. Acta Materialia, 2021, 220: 117310.

[5] LIU Tao, HU Guang-min, WANG Yu-jie, ZENG Jian-rong, DONG Qing, BIAN Feng-gang, CAO Zhao-peng, MENG Nan, ZHANG Jiao, SUN Bao-de. Investigation of precipitation strengthening behavior of Al−Mg−Si alloy using SAXS [J]. Transactions of Nonferrous Metals Society of China, 2023, 33: 1305−1317.

[6] LIU Shu-hui, WANG Xiang-dong, PAN Qing-lin, LI Meng-jia, YE Ji, LI Kuo, PENG Zhuo-wei, SUN Yu-qiao. Investigation of microstructure evolution and quench sensitivity of Al−Mg−Si−Mn−Cr alloy during isothermal treatment [J]. Journal of Alloys and Compounds, 2020, 826: 154144.

[7] LEI Gang, GAO Hai-tao, ZHANG Yun, CUI Xiao-hui, YU Hai-liang. Atomic-level insights on enhanced strength and ductility of Al−Mg−Si alloys with β''-Mg_5Si_6 at cryogenic temperatures [J]. Transactions of Nonferrous Metals Society of China, 2023, 33: 2943−2954.

[8] YANG Ming-jun, CHEN Hao-nan, OREKHOV A, LU Qiang, LAN Xin-yue, LI Kai, ZHANG Shu-yan, SONG Min, KONG Yi, SCHRYVERS D, DU Yong. Quantified contribution of β'' and β' precipitates to the strengthening of an aged Al−Mg−Si alloy [J]. Materials Science and Engineering: A, 2020, 774:138776.

[9] YAN Li-zhen, LI Zhi-hui, ZHANG Yong-an, XIONG Bai-qing, LI Xi-wu, LIU Hong-wei, HUANG Shu-hui, YAN Hong-wei. Pre-aging on early-age behavior and bake hardening response of an Al−0.90Mg−0.80Si−0.64Zn−0.23Cu alloy [J]. Progress in Natural Science: Materials International, 2016, 26: 398−403.

[10] POGATSCHER S, ANTREKOWITSCH H, LEITNER H, SOLOGUBENKO A S, UGGOWITZER P J. Influence of the thermal route on the peak-aged microstructures in an Al−Mg−Si aluminum alloy [J]. Scripta Materialia, 2013, 68: 158−161.

[11] TAO G H, LIU C H, CHEN J H, LAI Y X, MA P P, LIU L M. The influence of Mg/Si ratio on the negative natural aging effect in Al−Mg−Si−Cu alloys [J]. Materials Science and Engineering: A, 2015, 642: 241−248.

[12] SARUWATARI N, YASUE K, NAKAYAMA Y. Effect of reheating after low temperature pre-aging on microstructure of 6061 aluminum alloy [J]. Materials Transactions, 2022, 63: 286−293.

[13] STROBEL K, LAY M D H, EASTON M A, SWEET L, ZHU Su-ming, PARSON N C, HILL A J. Effects of quench rate and natural ageing on the age hardening behaviour of aluminium alloy AA6060 [J]. Materials Characterization, 2016, 111: 43−52.

[14] LAI Y X, JIANG B C, LIU C H, CHEN Z K, WU C L, CHEN J H. Low-alloy-correlated reversal of the precipitation sequence in Al−Mg−Si alloys [J]. Journal of Alloys and Compounds, 2017, 701: 94−98.

[15] CHANG C S T, WIELER I, WANDERKA N, BANHART J. Positive effect of natural pre-ageing on precipitation hardening in Al−0.44at.%Mg−0.38at.% Si alloy [J]. Ultramicroscopy, 2009, 109: 585−592.

[16] LIU C H, LAI Y X, CHEN J H, TAO G H, LIU L M, MA P P, WU C L. Natural-aging-induced reversal of the precipitation pathways in an Al−Mg−Si alloy [J]. Scripta Materialia, 2016, 115: 150−154.

[17] YANG Zi, LIANG Ze-qin, DAVID L, JOHN B. Effect of pre-ageing on natural secondary ageing and paint bake hardening in Al−Mg−Si alloys [J]. Materialia, 2019, 7: 100413.

[18] LI Gao-jie, GUO Ming-xing, DU Jin-qing, ZHUANG Lin-zhong. Synergistic improvement in bake-hardening response and natural aging stability of Al−Mg−Si−Cu−Zn alloys via non-isothermal pre-aging treatment [J]. Materials & Design, 2022, 218: 110714.

[19] KIM S N, SONG M Y, LEE J, KIM J H. The nanocluster formation and vacancy behavior of step- quenched Al−Mg−Si alloy and its effect on transition to β'' phase via advanced methods [J]. Materials Science and Engineering: A, 2021, 811: 141032.

[20] ENGLER O, MARIOARA C D, ARUGA Y, KOZUKA M, MYHR O R. Effect of natural ageing or pre-ageing on the evolution of precipitate structure and strength during age hardening of Al−Mg−Si alloy AA 6016 [J]. Materials Science and Engineering: A, 2019, 759: 520−529.

[21] ZANDBERGEN M W, XU Q, CEREZO A, SMITH G D W. Study of precipitation in Al−Mg−Si alloys by atom probe tomography: I. Microstructural changes as a function of aging temperature [J]. Acta Materialia, 2015, 101: 136−148.

[22] CUI Z J, JIANG H C, ZHANG D, SONG Y Y, YAN D S, RONG L J. Influence of Mn on the negative natural aging effect in 6082 Al alloy [J]. Materials Science and Engineering: A, 2020, 793: 139874.

[23] GAO G J, LI Y, WANG Z D, MISRA R D K, LI J D, XU G M. Study of retrogression response in naturally and multi-step aged Al−Mg−Si automotive sheets [J]. Journal of Alloys and Compounds, 2018, 753: 457−464.

[24] ZHU Su-qin, SHIH H C, CUI Xiang-yuan, YU Chung-yi, RINGER S P. Design of solute clustering during thermomechanical processing of AA6016 Al−Mg−Si alloy [J]. Acta Materialia, 2021, 203: 116455.

[25] GUO M X, LI G J, ZHANG Y D, SHA G, ZHANG J S, ZHUANG L Z, LAVERNIA E J. Influence of Zn on the distribution and composition of heterogeneous solute-rich features in peak aged Al−Mg−Si−Cu alloys [J]. Scripta

Materialia, 2019, 159: 5−8.
[26] LERVIK A, THRONSEN E, FRIIS J, MARIOARA C D, WENNER S, BENDO A, MATSUDA K, HOLMESTAD R, ANDERSEN S J. Atomic structure of solute clusters in Al−Zn−Mg alloys [J]. Acta Materialia, 2021, 205: 116574.
[27] ZANG Ruo-jin, WAN Bin, DING Li-peng, EHLERS F J H, JIA Zhi-hong, CAO Ling-fei, LI Yan-jun. The combined effect of pre-aging and Mg/Si ratio on the natural aging and bake hardening in Al−Mg−Si−0.7Cu alloys [J]. Materials Characterization, 2024, 212: 113987.
[28] WANG Shuai, LUO Bing-hui, BAI Zhen-hai, HE Chuan, JIANG Gen. Effect of pre-ageing on nucleating of GP zones and precipitation, strength and stress corrosion properties of 7N01 alloy [J]. Journal of Alloys and Compounds, 2024, 980: 173681.
[29] SONG M Y, KIM J H. Microstructural evolution at the initial stage of two-step aging in an Al−Mg−Si alloy characterized by a three dimensional atom probe [J]. Materials Science and Engineering: A, 2021, 815: 141301.
[30] PANDE C S, COOPER K P. Nanomechanics of Hall−Petch relationship in nanocrystalline materials [J]. Progress in Materials Science, 2009, 54: 689−706.
[31] KOCKS U F, MECKING H. Physics and phenomenology of strain hardening: The FCC case [J]. Progress in Materials Science, 2003, 48: 171−273.
[32] ESMAEILI S, LLOYD D J, POOLE W J. A yield strength model for the Al−Mg−Si−Cu alloy AA6111 [J]. Acta Materialia, 2003, 51: 2243−2257.
[33] DESCHAMPS A, BRECHET Y. Influence of predeformation and ageing of an Al−Zn−Mg alloy: II. Modeling of precipitation kinetics and yield stress [J]. Acta Materialia, 1998, 47: 293−305.
[34] SHISHIDO H, ARUGA Y, MURATA Y, MARIOARA C D, ENGLER O. Evaluation of precipitates and clusters during artificial aging of two model Al−Mg−Si alloys with different Mg/Si ratios [J]. Journal of Alloys and Compounds, 2022, 927: 166978.
[35] DONG Yan-hui, ZHANG Dan, LI Da-guang, JIA Heng, QIN Wei-ping. Control of Ostwald ripening [J]. Science China Materials, 2023, 66: 1249−1255.
[36] MEYRUEY G, MASSARDIER V, LEFEBVRE W, PEREZ M. Over-ageing of an Al−Mg−Si alloy with silicon excess [J]. Materials Science and Engineering: A, 2018, 730: 92−105.
[37] ARUGA Y, KOZUKA M, TAKAKI Y, SATO T. Evaluation of solute clusters associated with bake-hardening response in isothermal aged Al−Mg−Si alloys using a three-dimensional atom probe [J]. Metallurgical and Materials Transactions A, 2014, 45: 5906−5913.

自然时效和预时效对 Al−Mg−Si 合金时效硬化过程中显微组织演变和强化能力的影响

刘淑辉[1,2]，潘清林[3]，黄宏锋[1,2]，王 静[4]，李德贵[4]，宁志鑫[1]，韦莉莉[1,2]

1. 桂林理工大学 材料科学与工程学院，桂林 541004；
2. 桂林理工大学 有色金属及材料加工新技术教育部重点实验室，桂林 541004；
3. 中南大学 材料科学与工程学院，长沙 410083；
4. 百色学院 广西铝基新材料工程研究中心，百色 533000

摘 要：对 Al−Mg−Si 合金经自然时效(NA)、延迟时效(DA)和预时效+延迟时效(PDA)后的显微组织演变和强化能力进行研究。结果表明，在 NA 过程中产生了不稳定的小尺寸原子团簇，导致低密度且粗大的 β''和 β'相的形成，降低了 DA 合金的强度。然而，预时效处理过程中形成了大尺寸和高 Mg/Si 摩尔比的原子团簇和 GP 区，阻止了自然时效过程中原子团簇的产生，并在随后的人工时效过程中作为有效的析出相形核位置，提高了细小 β''析出相的数量密度，从而增强了合金的强度。经 175 ℃预时效处理后，PDA 合金的强化能力得到了恢复，其硬度和屈服强度分别达到峰值时效合金的 95.1%和 101.9%。

关键词：预时效；延迟时效；析出相；显微组织演变；强化能力；Al−Mg−Si 合金

(Edited by Wei-ping CHEN)